



The 2019 Ridgecrest, California earthquake sequence: Evolution of seismic and aseismic slip on an orthogonal fault system

Han Yue^{a,b,*}, Jianbao Sun^c, Min Wang^c, Zhengkang Shen^{a,d}, Mingjia Li^a, Lian Xue^a, Weifan Lu^a, Yijian Zhou^a, Chunmei Ren^a, Thorne Lay^e

^a School of Earth and Space Sciences, Peking University, Beijing 100871, China

^b Hongshan Geophysical National Observation and Research Station, Peking University, Beijing 100871, China

^c State Key Laboratory of Earthquake Dynamics, Institute of Geology, China Earthquake Administration, Beijing 100029, China

^d University of California, Los Angeles, CA, 90095-1567, USA

^e University of California Santa Cruz, Santa Cruz, CA, 95064, USA

ARTICLE INFO

Article history:

Received 26 September 2020

Received in revised form 1 June 2021

Accepted 16 June 2021

Available online 16 July 2021

Editor: J.-P. Avouac

Dataset link:

<https://doi.org/10.7909/C3WD3xH1>

Keywords:

Ridgecrest earthquake

co-seismic/afterslip models

seismic and aseismic slip

ABSTRACT

Cascade-up and/or slow-slip processes are commonly believed to control interactions between foreshocks, mainshocks and aftershocks, but their relative contributions remain poorly resolved. Discrimination between these processes will shed light on the understanding of earthquake physics, which requires exceptional observations of earthquake sequences. The well-recorded July 2019 Ridgecrest, California foreshock-mainshock-aftershock earthquake sequence provides such an opportunity. We perform simultaneous inversion of the July 4th M_W 6.4 foreshock and July 5th M_W 7.1 mainshock kinematic rupture models using SAR, strong motion, and GPS data. We also invert for afterslip models following the M_W 6.4 foreshock and the mainshock, respectively, by developing an inversion method that utilizes strainmeter, SAR and daily GPS time series. The inversion results show that the overall sequence involves no less than six fault segments, which include a main northwest-trending fault and secondary faults with sub-parallel and orthogonal geometry to the main fault. Co-seismic slip and afterslip have complementary patterns on the faults. During the early post-seismic period following the M_W 6.4 foreshock and the mainshock, moment release on the southwest-trending fault is dominated by aseismic slip, in contrast to the predominantly seismic slip on the northwest-trending fault. The mainshock appears to be triggered by a cascade migration of foreshocks on a northwest-trending fault. Slip on the southwest-trending fault migrates from the fault junction at the northeast end (following the M_W 6.4 foreshock) to the southwest end (following the mainshock) during the afterslip interval. The dual-mode (seismic versus aseismic) slip phenomena appear to be driven by co-seismic stress changes produced by the major events.

© 2021 Elsevier B.V. All rights reserved.

1. Introduction

Earthquakes are almost always followed by smaller earthquakes (aftershocks), and some earthquakes are preceded by smaller events (foreshocks) (e.g., Jones and Molnar, 1979; Trugman and Ross, 2019; Ende and Ampuero, 2020). Foreshock sequences are a precursory phenomenon that could potentially be used to forecast the mainshock occurrence, yet the triggering mechanism is not fully understood. The behavior of foreshock sequences can be classified into two end-member groups, i.e. the “cascade-up” model and the “slow-slip model”. From an observational perspective, the

cascade-up model assumes “earthquakes produce earthquakes”, and emphasizes stress interactions between adjacent foreshocks, that finally lead to the rupture of the mainshock (e.g., Ellsworth and Bulut, 2018; Yoon et al., 2019). The slow-slip model assumes that “slow-slip produces earthquakes” (Dieterich, 1979) and identifies stress loading by slow-slip as the dominant process driving foreshocks, which in turn provide indicators of the slow-slip (e.g., Kato et al., 2012). In practice, afterslip following a large foreshock can act as a slow-slip process driving the foreshock sequence, even if no slow-slip preceded the first foreshock. In laboratory experiments, both contributions can be important for controlling the occurrence time of a mainshock (McLaskey, 2019). The accumulated case studies of earthquake sequences over the past few decades suggest that both foreshock processes can operate and may comparably account for basic seismic and geodetic observations (Ruiz et al., 2014; Schurr et al., 2014). However, it is generally

* Corresponding author at: School of Earth and Space Sciences, Peking University, Beijing 100871, China.

E-mail address: yue.han@pku.edu.cn (H. Yue).

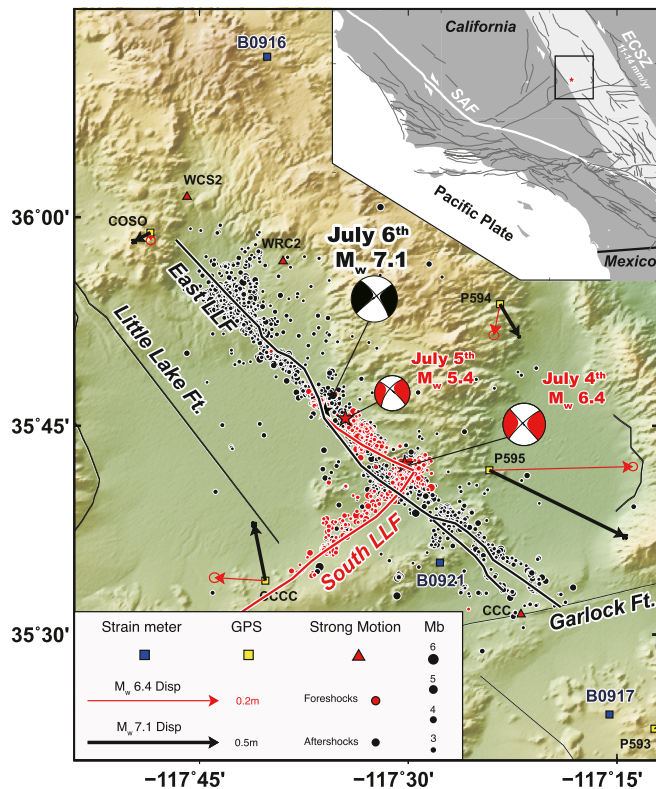


Fig. 1. Regional tectonic map and earthquake information. GCMT solutions for the M_w 6.4 and 5.4 foreshocks and the mainshock are plotted with red- and black-filled focal mechanisms respectively. Foreshocks and aftershocks are plotted with red- and black-filled circles, respectively. Identified foreshock and mainshock fault traces are plotted as red and black curves, respectively. Strainmeters (blue squares), GPS (yellow squares), and strong motion stations (red triangles) are plotted. GPS horizontal displacements of the M_w 6.4 foreshock and the mainshock are plotted in red and black arrows, respectively. Regional faults are plotted as black curves and labeled. The regional tectonic map for southern California is plotted on the top right. The main figure area is indicated by a black box. The Eastern California Shear Zone (ECSZ) is indicated by a white swath. The northwest-trending fault is now called the Eastern Little Lake Fault (East LLF), and the southwest trending fault is now called the Southern Little Lake Fault (South LLF). (For interpretation of the colors in the figure(s), the reader is referred to the web version of this article.)

difficult to discriminate the contribution of either mechanism for specific earthquake interactions.

Here, we study the July 2019 Ridgecrest, California (RC) earthquake sequence, which involved a foreshock sequence rupture of two mutually perpendicular faults. Exceptional data indicate that during the foreshock sequence, both cascade-up and slow-slip processes occurred, but distinctly on the orthogonal faults. The cascade process appears to have been the dominant mechanism involved in mainshock triggering along the primary fault system, while the slow slip process (afterslip of the largest foreshock; no earlier slow slip has been detected) is the dominant mechanism driving deformation and aftershocks on the perpendicular fault.

The RC sequence (Fig. 1) initiated with an M_w 6.4 foreshock, followed by numerous aftershocks, including an M_w 5.4 event that occurred to the northwest of the foreshock epicenter with ~ 19 -hour delay. The M_w 7.1 mainshock occurred near the M_w 5.4 hypocenter ~ 15 hours later. The mainshock is the largest earthquake in California in the last 20 years. The Ridgecrest earthquake caused an economic loss of about five billion dollars (Hough et al., 2020). The three largest events have strike-slip focal mechanisms consistent with a right-lateral sense of offset for a northwest-striking fault. The aftershock distribution indicates the overall rupture extent and demonstrates that the M_w 6.4 foreshock likely

ruptured two orthogonal faults, while the mainshock occurred on a ~ 50 km long NW-trending segmented fault system.

The seismogenic faults are situated in the Indian Wells Valley in eastern California, and the two orthogonal faults, which were not recognized prior to the 2019 sequence, are now named the NW-trending Eastern Little Lake and SW-trending Southern Little Lake faults. These faults are among an ensemble of faults in the Eastern California Shear Zone (ECSZ), which is a deformation belt ~ 100 km wide extending from the Mojave Desert in southern California to northwestern Nevada (Dokka and Travis, 1990; Savage et al., 1990; Unruh et al., 2003). Dextral shear motion of ~ 11 -14 mm/yr has been measured by GPS across this part of the ECSZ, but the strain is broadly distributed in the deformation zone, and its partitioning among faults has been a subject of investigation (e.g., Gan et al., 2000; McClusky et al., 2001; Miller et al., 2001). No anomalous strain gradient had been detected previously across the two faults involved in the RC sequence, which were only partially mapped before this event.

Rupture processes of the RC earthquake sequence have been investigated using seismic and geodetic observations jointly or separately, (e.g., Chen et al., 2020; Goldberg et al., 2020; Liu et al., 2019; Magen et al., 2020; Ross et al., 2019; Wang et al., 2020). Because the foreshock and mainshock deformation is mingled in SAR images, it is challenging to incorporate this high-resolution data in the joint inversion. Wang et al. (2020) and Chen et al. (2020) used similar strategies, which invert for one major event first and then invert for the other event using the remnant displacement field. Magen et al. (2020) and Goldberg et al. (2020) concatenate Green's functions of the mainshock and foreshock in a uniform matrix and perform simultaneous inversion using SAR and optical images and static GPS data, while seismic data are also used by Goldberg et al. (2020). The interactions between foreshock co-seismic slip, afterslip and seismic events following the M_w 6.4 foreshock, and the mainshock can shed light on earthquake physics, and require an integrated analysis of the slip processes. We perform simultaneous linear inversion to resolve the kinematic rupture process of both major events by the joint use of GPS, SAR, and strong motion observations. We consider the afterslip following the M_w 6.4 foreshock and mainshock as quasi-static processes and develop a linear inversion method to invert for the temporal evolution. The relationship between these processes and associated physics in this complicated fault system is discussed.

2. Data and methods

2.1. Fault model construction

The RC earthquake sequence occurred in a densely instrumented area of California. Seismic waves from the M_w 6.4 foreshock and the M_w 7.1 mainshock ruptures were recorded by regional strong-motion and high-rate GPS (hr-GPS) stations, and cumulative static displacements of the sequences were captured by daily GPS and synthetic aperture radar (SAR) measurements. For performing linear inversions for space-time slip distributions a pre-determined fault geometry is required to calculate Green's functions. Alternatively, geometrical fault parameters also need to be inverted using a non-linear approach. In this study, we adopt a similar strategy to Yue et al. (2017), relying on surface fault traces and depth distribution of aftershocks to parameterize a multi-segmented and curved fault system used in linear inversions.

The SAR satellites scan the ground periodically, and the deformation that occurs between two scans can be derived from the data, providing the highest spatial resolution among all available data. For the RC earthquake sequence, all SAR measurements were made before the foreshock and after the mainshock, such that the interferograms depict the superimposed co-seismic displacement

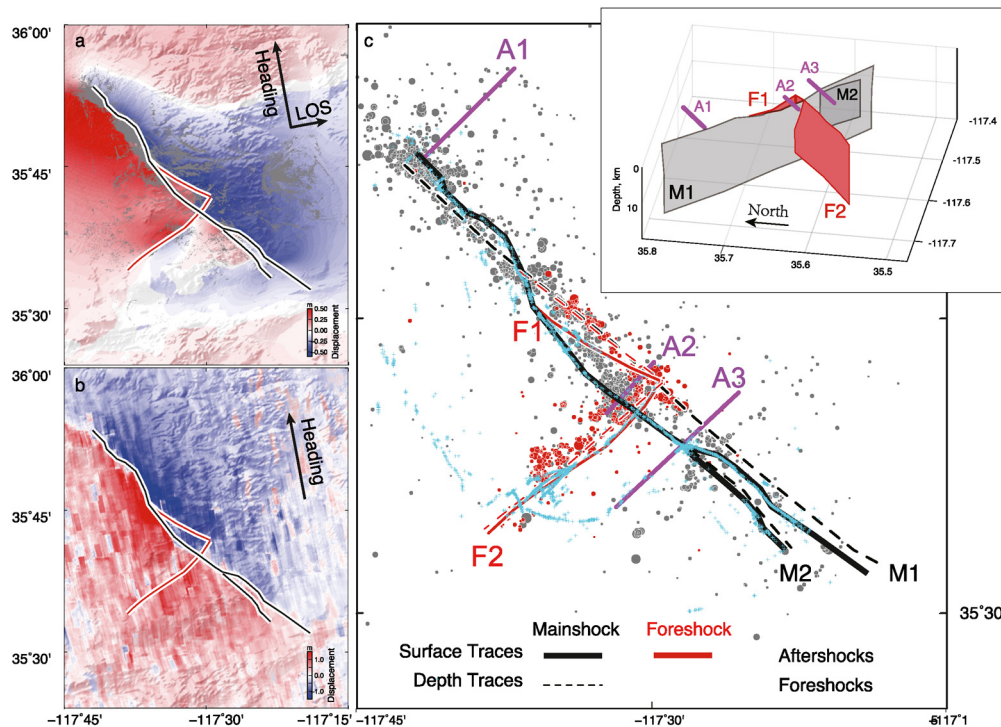


Fig. 2. Fault surface trace and 3D geometry. **a, b** Example **A064** S1 ascending SAR interferogram and azimuth offset data (see Fig. S2 for additional data). The cumulative deformation in the interferometric pair date from July 4 to July 10 (Table S1) displacement field projected to the SAR Line-of-Sight and heading direction is plotted with a blue to red color scale. The satellite heading and look directions are plotted with black arrows. **c.** Foreshocks and aftershocks are plotted as magenta and gray filled circles, respectively. In all three panels, surface fault traces are plotted as red and black curves, respectively. Field-observed surface ruptures are marked as cyan crosses. Deep edges of the foreshock and mainshock faults are plotted as red and black dashed curves, respectively. Inferred 3D fault planes are plotted as red and gray filled planes in the top-right inset.

field of the foreshock, the mainshock, and their early aftershocks, along with any aseismic slip during the interferometric pair dates (see Table S1). We use both the C-band SAR data from Sentinel-1 (S1) satellites of the European Space Agency (ESA) and the L-band PALSAR-2 data of ALOS-2 satellite from the Japanese Aerospace Exploration Agency (JAXA). Interferometry (Strozzi et al., 2008) and offset tracking (Leprince et al., 2007) methods were used to process SAR images to obtain co-seismic ground deformation. Surface rupture traces are manually picked from azimuth-offset images. Details of SAR data processing are described in the supplementary materials. Surface ruptures measured by field investigation (DuRoss et al., 2020) are consistent with the surface offsets depicted by SAR images (Fig. 2).

The observed surface offsets are used to parameterize the fault model; however, many smaller features may be very shallow secondary fractures triggered by the mainshock. Including these trivial structures provides very limited information about the mainshock rupture and expands the model space to explore, which is inconvenient for inversion and parameter tuning. We desire the fault model to capture the primary rupture pattern without emphasizing secondary surface ruptures to keep the slip model relatively simple and representative of the robust faulting at depth. Three criteria are considered when dismissing secondary fault traces:

- (1) traces less than 5 km long.
- (2) traces located further than 5 km from the main rupture trace.
- (3) traces lacked seismicity lineation.

Following these criteria, we identify four major surface rupture traces from field observations and SAR images and use them to parameterize the fault model. We consider these four traces as primary fault segments hosting the foreshock and mainshock (Fig. 2).

We use seismicity locations to determine fault geometries at depth. The catalog of Shelly (2020) is used to construct the fault

model and calculate seismic moment release since it is the first catalog available to us. We assume the foreshock occurred on two fault segments F1 and F2 (Fig. 2), both showing about 10 km lateral extent and forming an orthogonal structure. The mainshock aftershocks cover a larger lateral extent (~30 km). The mainshock involves two NW-SE trending faults M1 and M2, where M2 is a smaller branch at the southeast end of M1. The surface trace of segment M1 is curved in its central segment, but its profile at depth is relatively straight.

Two additional fault planes, A1 and A2, are included in the afterslip model with respect to the observed offsets on the ground surface. They are connected to fault M1 at its northwestern end and cut M1 in the center (Fig. 2), respectively. The main fault plane (M1) extends to 29 km depth for afterslip modeling, in comparison with a shallow depth limit (20 km) for the co-seismic fault model. This parameterization allows us to explore deep afterslip beneath the seismogenic depth. Details of the fault geometry are documented in the supplementary materials (Table S3), and the detailed sub-fault parameters are provided in the inversion results. Several studies include segment A2 in the kinematic rupture process inversion, e.g., Ross et al. (2019), Wang et al. (2020), and Goldberg et al. (2020). Seismicity on A2 was most active during the aftershock sequence rather than in the foreshock sequence, indicating that this structure was activated by the mainshock rupture. In comparison with the extended slip on M1 and M2 during the mainshock, this short structure is not a significant feature. Thus we do not include this segment in our co-seismic slip model.

2.2. Joint inversion of M_W 6.4 foreshock and mainshock rupture processes

We conduct a joint inversion for the kinematic rupture process of the foreshock and mainshock. Eight SAR images obtained by interferometry, range-offset, and azimuth offset of Sentinel-1 and

ALOS2 satellite are used in the joint inversion. Because the time intervals of these SAR images span the occurrence of both M_W 6.4 and 7.1 events, they depict the cumulative ground deformation produced by both major events. We also use static and high-rate GPS data in the joint inversion technique. Three-component ground displacements of 31 and 42 static GPS stations are used to invert for the foreshock and mainshock co-seismic slip distributions, respectively. Three-component ground displacement time series from 5 and 20 hr-GPS stations are used to constrain the rupture processes of the foreshock and mainshock, respectively. The original displacement time-series are converted to velocities before use in the inversion algorithm. The velocity waveforms are band-pass filtered with corner frequencies of 0.02 and 0.25 Hz, and cut with 50 s long time-windows starting at the earthquake initial time at one sps interval. We also use three-component acceleration recordings from 10 strong-motion stations and calculate ground velocity waveforms by integrating the original data. The strong motion data are filtered between 0.05 and 0.25 Hz. Details of data processing and visualization are available in the supplementary materials.

Joint use of SAR, GPS and seismic data exploits their respective resolution of different source rupture features, and thus can provide a more robust slip model (Yue et al., 2020). However, it is not straightforward to directly adopt all data types in the inversion because the displacement fields of the M_W 6.4 foreshock and the M_W 7.1 mainshock are superimposed in the SAR images, yet separated in the GPS and kinematic observations. Based on a traditional multi-time-window inversion algorithm (Hartzell and Heaton, 1983), we design a linear inversion algorithm to simultaneously invert for the foreshock and mainshock space-time slip evolution using the above available data. This algorithm uses respective static and kinematic data to constrain the rupture process of individual events, while still keeping summation of their co-seismic displacements to be consistent with the SAR observations. We parameterize the ruptured faults as the foreshock and mainshock segments and then calculate Green's functions of each observation for the inversion parameters. Green's functions of the foreshock and mainshock are concatenated at diagonal locations of the inversion matrix to enable respective fits to GPS and strong motion data of either event, while SAR Green's functions are concatenated in the row direction to account for the cumulated contribution to the SAR observations. This inversion design is similar to that used by previous studies (Yue et al., 2017; Goldberg et al., 2020; Magen et al., 2020). Details of the inversion matrix design and relative data weighting are described in detail in the supplementary materials. The mainshock hypocenter is set at 3 km depth, as reported by Shi et al. (2019), who calibrated the initial arrival time using a regional event. The choice of hypocenter depth at 3 km does not influence the slip model significantly, but improves waveform fits to the initial strong-motion arrivals relative to deeper positions. We also incorporate damping operation for slip spatial roughness and boundary slips. The boundary damping reduce slips near the fault side and bottom edges, where model resolution is relatively low. Although slips on most boundaries are cleaned by the boundary damping, we consistently resolve some slips at the bottom of F2 near its junction side under the same damping level. This phenomenon indicates such rupture patch may be required to fit data, while more studies are needed to discuss its implication for rupture dynamics.

2.3. Strainmeter time series of deformation following the M_W 6.4 foreshock

To investigate the triggering mechanism between the M_W 6.4 foreshock and the mainshock, we make use of the regional strainmeter recordings to resolve the slip process during this period. The

slip that occurred between the M_W 6.4 foreshock and the mainshock is comprised of both seismic slip (additional foreshocks) and aseismic afterslip. Resolving slow slip evolution requires ground deformation measurements that capture quasi-static responses to fault slip recorded at a high temporal sampling rate. This requirement excludes the use of seismic and SAR data for this purpose. We also do not find GPS displacement signals above the noise level in the period between the M_W 6.4 foreshock and the mainshock (as also reported by Wang et al., 2020). Fortunately, the deformation during the foreshock sequence was clearly recorded by near-field strainmeter stations (Fig. 1). Station B0916 is located north of F1, and station B0921 is close to F2; thus, their strain measurements are primarily sensitive to the slip history of F1 and F2, respectively. Each strainmeter records time series of 3 plane strain components of the full 6 component strain tensor, ϵ ; ϵ_{ee} , ϵ_{nn} , and ϵ_{en} . The plane strain tensors are shown as rotated "cross" symbols in Fig. 4, which depict pairs of eigenvalues oriented in the directions of orthogonal eigenvectors. We use three stations including B0916 and B0921 to analyze the slow-slip process following the M_W 6.4 foreshock.

The data from B0916 clearly show several sharp jumps. In contrast, the time series at B0921 show a smooth logarithmic decay (Figs. 4 and 5). Considering the locations of B0916 and B0921, these time series data suggest that deformation on F1 and F2 following the M_W 6.4 foreshock may be dominated by episodic "cascade slip" and steady "slow slip", respectively (Fig. 1). We isolate strain jumps caused by the M_W 5.4 event in the two strainmeter observations, and use a point source focal mechanism to predict similar strain tensors to the observations as a test. We also perform a linear inversion for slip distribution on F1, which estimates an M_W 5.36 event at the northwest end of F1, consistent with the actual M_W 5.4 event location (Fig. S20). The reasonable results found for that event give us confidence to use the strain observations to quantitatively determine the overall deformation process including any slow-slip. We adopt the full time series inversion method to these strainmeter data to investigate the afterslip following the M_W 6.4 foreshock. Details of the inversion method are presented in later sections.

2.4. Observations of post-seismic deformation

We also investigate the afterslip process that occurred within six months after the mainshock (July 6th - Dec 31st, 2019). Three types of data are used in this inversion, including GPS, SAR interferogram, and strainmeter time series. We use daily solutions of ground displacements recorded by 21 regional GPS stations, with a time window starting 50 days (May 17th, 2019) before the mainshock and ending 150 days (Dec 3rd 2019) after the mainshock. The daily GPS time series are recorded by the plate boundary observatory network (PBO) and accessed through UNAVCO. The original solutions are fitted by a combination of several synthetic functions, i.e. a linear trend, co-seismic steps of the foreshock and mainshock, and a post-seismic (logarithmic) trend. The linear trend and co-seismic steps are then removed from the original displacement time series. The GPS data for the days of the foreshock and mainshock are not used in the inversion, because it requires separate processing to estimate the displacements before and after the events.

The SAR images include 27 and 22 frames for ascending and descending orbits, respectively. The original SAR images are down-sampled into 576 and 686 pixels for the ascending and descending orbits, respectively, using the identical sampling method as the co-seismic images. For each of the SAR images, we correct the linear trend referenced to GPS displacements. The vertical components of the GPS data are not used for the ramp estimation, because errors of the vertical components are often greater than the sig-

nal, and their inclusion may cause larger error (Fig. S22) in the ramp estimation (Shen and Liu, 2020). In addition to the afterslip, viscous relaxation also contributes to the post-seismic ground deformation, which needs to be accounted for before performing slip inversions. We use a regional visco-elastic model (Liu et al., 2020) to simulate the post-seismic relaxation caused by the mainshock. The relaxed displacement field is calculated by a 1D-layer simulation code (Wang et al., 2006) at the GPS/SAR data sampling locations, and then removed from the GPS/SAR time series. A comparison between the synthetic relaxed and corrected displacement fields is plotted in Figs. S21 and S23.

To resolve the deformation that occurred immediately after the mainshock, we adopt the three-component plane-strain time series of station B0921 in the afterslip inversion. The other two stations were either not functioning (B0916) or dominated by slip on the Garlock fault (B0917), thus they are not used in the inversion. Original strain time series of station B0921 are cut from 1 hour after the mainshock to 16 hours after the mainshock to enable monitoring of early afterslip. The strain data processing is identical to that used in the slow-slip inversion after the M_W 6.4 foreshock.

2.5. Full time series inversion for afterslip following the M_W 6.4 foreshock and afterslip following the mainshock

SAR time series provide the highest spatial resolution and lowest temporal resolution. GPS data are daily sampled at discrete locations. Strainmeter data provide immediate monitoring of afterslip at 1-minute level sampling, though its long-term recording may suffer from baseline shifts. Incorporating different types of ground deformation time series introduces a challenge to the task of afterslip inversion. Traditional inversion algorithms treat the time series as segmented data, which extract the differential displacements from displacement time series to invert for the associated slip pattern (e.g., Bedford et al., 2013; Moreno et al., 2010), or decompose the displacement time series as principal components, which separates signal and noise in different components (e.g., PCAIM, Kositsky and Avouac, 2010). For the afterslip inversion following the M_W 6.4 foreshock, we test the PCAIM algorithm in our initial attempt but find that the sparse spatial sampling of strainmeter stations does not allow a complete separation of deformation signal and noise in different principal components. For the post-seismic period, these data have different sampling times and temporal coverage, introducing challenges to incorporate principal component analysis. Thus we develop a full time series inversion (FTI) algorithm, which assumes a uniform slip evolution function for all patches and uses all sample points of the time series in the inversion. The evolution function is described by Equation (1):

$$\mathbf{S}(t) = \mathbf{S}(t, t_0, \tau) = \begin{cases} \mathbf{0}, & \text{for } t < t_0 \\ \log\left(\frac{t-t_0}{\tau} + 1\right), & \text{for } t > t_0 \end{cases} \quad (1)$$

where t_0 is the earthquake initiation time and τ is the characteristic decay time. Since the source evolves slowly in the afterslip period, we adopt the quasi-static approximation and calculate the displacement/strain evolution function at the data sample time, for the purpose of combining different datasets in a linear inversion framework. "Full" in the acronym is reflected in two aspects: firstly, all sampling in a time series can be used instead of segmented time; secondly, data with different temporal samples or spans can be adopted in a joint inversion framework. The characteristic decay time τ is the only hyper-parameter that needs to be assumed before performing an inversion. We can perform inversion under different decay times and obtain the optimized value from a trade-off curve of the smooth level versus residual RMS (Fig. S24-S25). This approach resembles that used to determine rupture velocity

in the multi-time-window inversion. A similar strategy assuming logarithmic decay functions to realize the time series inversion was initially proposed by Liu and Xu (2019), which combined a Heaviside and logarithmic function to perform joint inversion of co-seismic and post-seismic slip using SAR time series. Our tests find that the advantages of the FTI inversion include:

1. Using full time series reduces the estimation errors. If the assumed source evolution function is a valid representation of afterslip processes, the adopted inversion technique essentially uses all sample points to estimate one parameter (total amplitude), which is more robust to the observational errors in comparison with segmented data inversion.
2. The FTI inversion is more flexible to incorporate different data in a joint inversion. Because the evolution function can be arbitrarily calculated at different sample times, it is straightforward to combine strainmeter, GPS, and SAR data in a joint inversion scheme. To determine early afterslip of the RC sequence requires combining the early afterslip sampling of strainmeter data, long base-line displacement recording of GPS data, and high spatial sampling of SAR data in a joint inversion scheme, which is the main motivation for developing this inversion technique.
3. The FTI inversion allows handling slow-slip processes with different initial times and decay time scales. Such inversion can be realized by parameterizing Green's functions with different source evolution functions and perform simultaneous linear inversion under the same framework. We also test two-process afterslip inversion for the RC sequence, which is discussed in the following sections.

Besides the common evolution function assumption, special treatments of SAR image correction and initial frame error correction are made in the inversion matrix reconstruction. We include more details of inversion matrix correction in the supplementary materials.

We adopt the FTI inversion algorithm and use the strainmeter time series of stations B0916, B0917, and B0921 to invert for the afterslip on the foreshock faults (F1 and F2) following the M_W 6.4 foreshock. The strain step-change associated with the M_W 5.4 event is removed from the original strain time series, and station B0921 presents a smooth evolution curve demonstrating that it is valid to use a presumed logarithmic decay function. Because the strainmeter data are limited, with only three stations and three components at each station being available, regularization is adopted in the inversion, including Laplacian smoothing of slip. We assume that slip on the sub-faults ruptured by the M_W 6.4 foreshock is limited to the period between the M_W 6.4 foreshock and the mainshock; thus we include slip damping for these sub-faults.

3. Results and discussion

3.1. Kinematic slip model of foreshock and mainshock

The kinematic slip models of the M_W 6.4 foreshock and the M_W 7.1 mainshock are visualized in Fig. 3. The kinematic slip models demonstrate that the M_W 6.4 foreshock initiated at the junction between F1 and F2, in the vicinity of a slip concentration on F1. The foreshock rupture expanded to the southwestern end of F2, with a heterogeneous slip distribution. The mainshock shows a downward and bilateral rupture propagation dominated by southeastward expansion. The peak slip is approximately 8.0 m at ~ 7.0 km depth in the vicinity of the hypocenter. The total seismic moment of the mainshock is 5.4×10^{19} N·m, which gives $M_W = 7.09$, consistent with the long-period point-source magnitude. The rupture velocity of the mainshock is determined to be

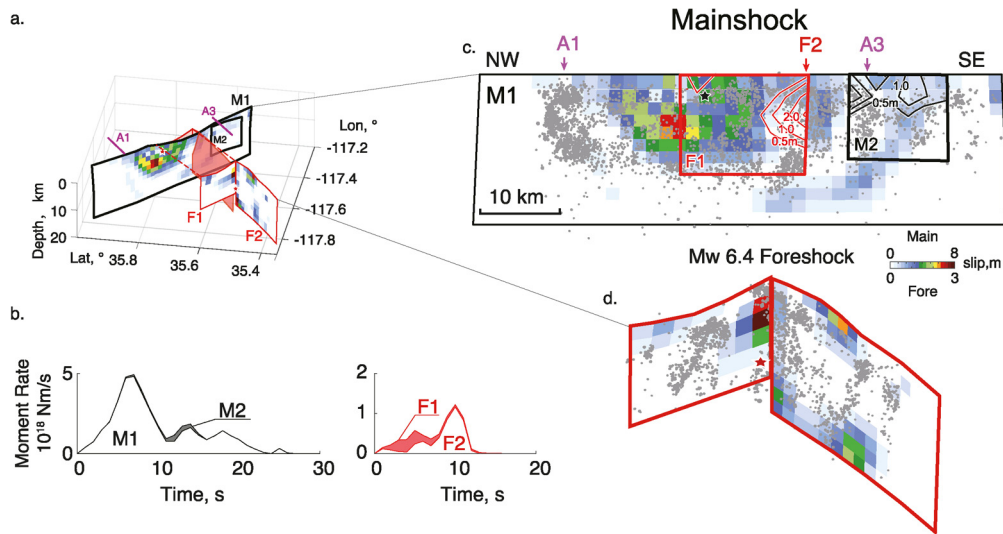


Fig. 3. Spatial and temporal slip evolution. **a.** Foreshock and mainshock slip distributions are plotted in color in a 3D view. The M_w 6.4 foreshock model is shifted for better visualization. **b.** Moment rate functions of the mainshock and M_w 6.4 foreshock are plotted with black and red polygons, with the contribution of each segment labeled. Contributions of slip on M2 and F1 are plotted as gray and red filled polygons. **c.** Slip distribution for the M_w 7.1 mainshock on fault M1 is plotted as a base color map. The mainshock hypocenter is indicated by the black star. Aftershocks are projected onto the slip pattern. Slip on F1 and M2 are plotted as red and black contours projected onto M1. **d.** The M_w 6.4 foreshock slip distribution on F1 and F2 is plotted in a 3D view. The M_w 6.4 hypocenter is indicated by the red star. The hypocenters of the M_w 5.4 and mainshock are plotted as black stars. Small foreshocks are plotted as gray-filled circles projected on the slip pattern.

~ 1.8 km/s, which is relatively low for strike-slip events. Hypocentral locations of the smaller seismicity (including foreshocks and aftershocks) are largely complementary to the slip distributions of the foreshock and the mainshock (Fig. 3). The overall slip pattern is consistent with those reported by other groups (e.g., Chen et al., 2020; Goldberg et al., 2020; Liu et al., 2019; Magen et al., 2020; Ross et al., 2019; Wang et al., 2020), although subtle details differ, in part due to varying fault parameterizations and data selection. Although shallow slip deficits are significant above the concentrated slip area, e.g., near the hypocenters of the M_w 6.4 foreshock and mainshock; many segments have peak slip at shallow depths, e.g., at the northwest ends of the main and parallel faults (M1 and F1) and the central segment of the orthogonal fault (F2). Several slip voids are observed on the main fault, the loci of which are associated with cross faults. The mechanism causing such slip voids is discussed later. We also make a forward prediction for the lateral displacements observed by several near-field campaign GPS stations (Floyd et al., 2020) using our kinematic slip models (Fig. S17). The foreshock co-seismic displacements are generally well predicted by our foreshock slip model. There are minor discrepancies between the predictions and observations for the mainshock displacements. Detailed analysis is available in the supplementary materials.

3.2. Slip following the M_w 6.4 foreshock and cascade triggering of the mainshock

Inversion results for slow deformation following the M_w 6.4 foreshock are shown in Fig. 4, with most slip located on the SW-trending fault (F2) near its junction with the NW-trending fault (F1). Moderate slip is obtained on F1 and near the southwest end of F2, yielding a total moment magnitude of $M_w = 5.64$. In order to test the data sensitivity, we divide the foreshock faults into three segments (Fig. 4): Seg1 (whole F1), Seg2 (NE half of F2), and Seg3 (SW half of F2), and perturb the total moment on each segment to test for the impact on data fits. When perturbing slip of each segment, we keep the slip pattern of each segment unchanged and multiply a scaling factor to all sub-fault slip values to generate slip models with different moments. The associated synthetics are then compared with the observations. The residual

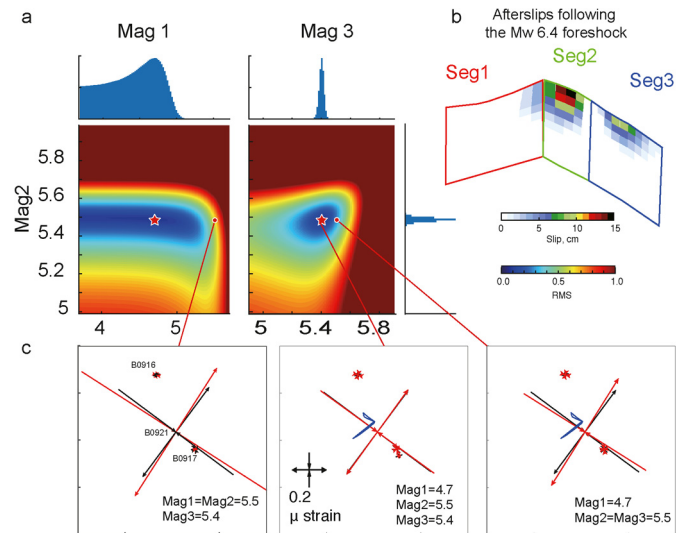


Fig. 4. Inversion results for afterslip following the M_w 6.4 foreshock. **a.** Residual distributions are plotted in a blue-red color scale in the segment distribution domain for Mag1 versus Mag2 and Mag3 versus Mag2 in the left and right panels, respectively. Scales of each segment are denoted in Fig. 4b. The marginal distributions of the magnitude of each segment are plotted as histograms in the top and right panels, respectively. **b.** Afterslip distribution (M_w 5.5 event removed) is plotted as a white-black color scale. **c.** Synthetic plane strain tensors computed by different combinations of segment magnitudes are plotted as red arrows in each panel. Observed plane strain tensors are plotted as black arrows. The equivalent magnitudes of each segment are labels and connect to the location in Fig. 4a.

distribution and synthetic comparisons are plotted in Figs. 4a and 4c. The preferred moment magnitudes on the three segments are 4.7, 5.5, and 5.4, respectively. Setting the moment magnitude of segments 1 and 3 (Mag1 and Mag3) to 5.5 (matching the magnitude of segment 2, Mag2) produces significant amplitude change and rotation of the B0921 strain tensor; thus the slip resolution on each segment mainly originates from the direction and amplitude at station B0921. We assume the observational error is about 10% of the maximum strain amplitude and calculate the probability density function of each magnitude and the residual distribution (Fig. 4a). The marginal distributions of magnitudes show

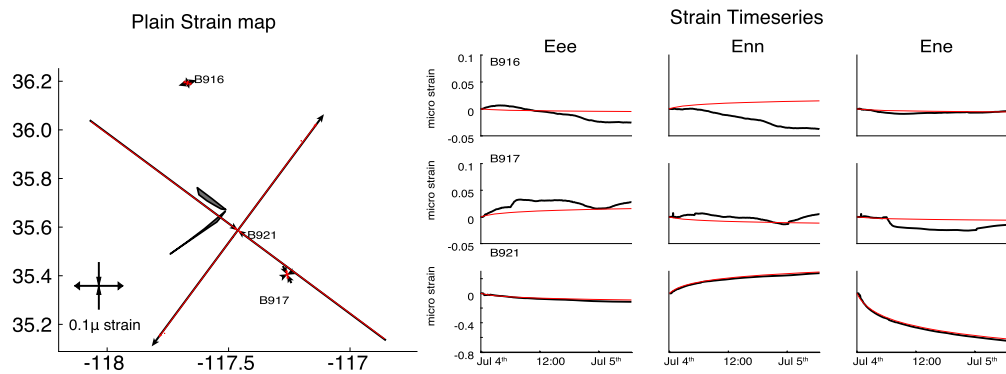


Fig. 5. Strainmeter data and model fitting. **a.** Observed and synthetic plane strain tensors plotted as black and red arrows, respectively. The foreshock fault planes (F1 and F2) are plotted as black polygons. **b.** Observed and synthetic strain time series are plotted as black and red curves, respectively. Row panels plot the strain time series of each station, and column panels plot the strain time series of each component, respectively.

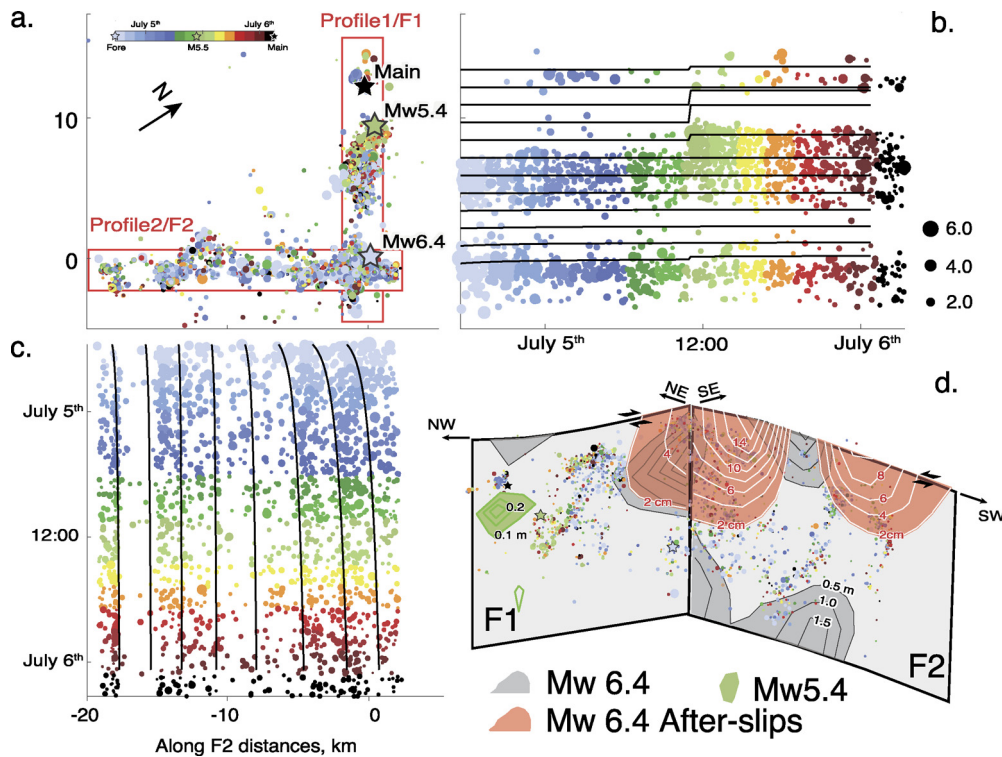


Fig. 6. Spatio-temporal evolution of seismicity and slip on faults during the foreshock period. **a.** Foreshocks are plotted as dots, color-coded by their occurrence time. Map orientation is rotated to the strike direction of F1. Two profiles are drawn along F1 and F2 to visualize their respective seismicity evolution. **b.** Foreshock distribution along the F1 strike direction is plotted as dots with occurrence time marked by color. Accumulated moment of the fault slip inverted by strainmeter time series is integrated along depth and plotted along the strike direction as black curves. **c.** Similar to **b** for the foreshock distribution along F2. **d.** M_W 6.4 foreshock slip and the post- M_W 6.4 slip are plotted as gray and red slip areas, respectively. The slip pattern of the M_W 5.5 foreshock is plotted as green contours. The foreshocks are plotted as dots, color-coded by their occurrence time with the same color scale as in **a**.

that Mag_2 is well constrained between 5.45 and 5.55. Mag_1 shows larger uncertainty, while the upper limit of Mag_1 is constrained to be < 5.1 . Thus slip on F1 (Mag_1) is significantly smaller than that on F2 ($Mag_2 + Mag_3$). Data fitting of the strainmeter observations is plotted in Fig. 5 in both map view and with temporal evolution function. It is noted that the strain amplitude of B0921 is one order of magnitude larger than that of the other two stations, which provides most constraints on the afterslip following the M_W 6.4 foreshock. The strain time series of B0916 and B0917 suffer from local noise, and the model only fits the general shape and amplitude.

Recalling that the M_W 5.4 event is removed from the strain time series and the remnant slip on F1 is less than M_W 5.1, we find that the M_W 5.4 event dominates the total moment release on F1 in the period between the M_W 6.4 event and the main-

shock. To compare the seismic and aseismic slip in the period between the M_W 6.4 event and the mainshock, we plot the foreshock distribution and migration on F1 and F2 in Fig. 6, which shows different foreshock migration patterns along the strikes of the two faults. The foreshocks on F2 initiated immediately after the M_W 6.4 foreshock along its full length (Fig. 6c). No significant jumps are found in the lateral afterslip migration pattern on F2. The foreshock activity on F2 decayed with time following a typical power-law decaying pattern (Omori law) up to the time of the mainshock when activity on F2 abruptly reduced. The stress control on F2 seismic activity is discussed in a later section. The foreshock activity on F1 was concentrated at its southeast half in the first 19 hours after the M_W 6.4 foreshock. The M_W 5.4 event ruptured a previously quiescent segment on the northwest edge of F1 and increased the surrounding seismic activity (Fig. 6).

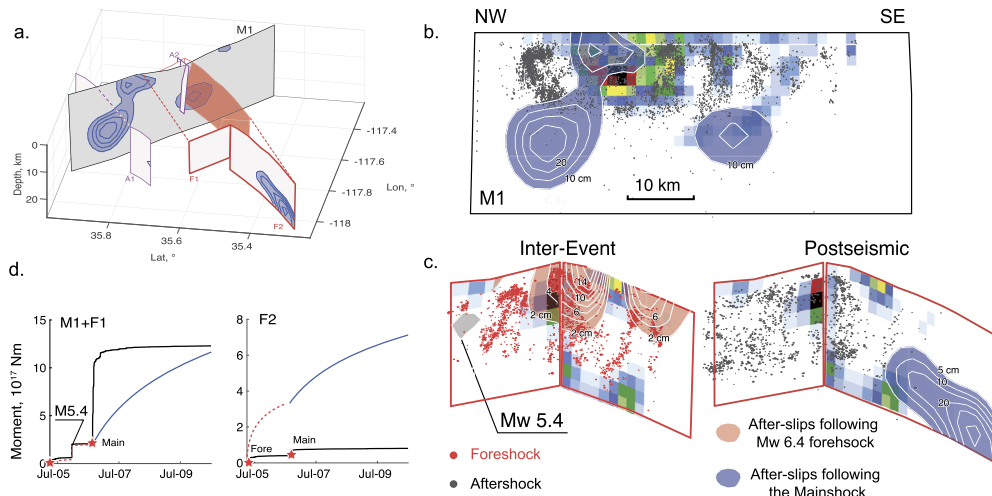


Fig. 7. Spatio-temporal evolution of seismicity and slip on faults from foreshock to post-seismic period. **a.** Spatial geometry of faults used in the post-seismic slip model is plotted as black (M1 and M2), red (F1 and F2) and magenta (A1, A3) polygons. The main afterslip areas are illustrated by blue contours. **b** and **c.** Similar to Fig. 3b and 3c. Afterslip areas are marked as blue contours. Afterslip areas following the M_w 6.4 foreshock are plotted as red contours. Foreshocks and aftershocks are plotted as red and black dots, respectively. **d.** Evolution functions of moment release on NW trending faults (M1 and F1) and SW trending faults (F2) are plotted in each panel, respectively. Catalog moment release is plotted as black curves. Moment release of afterslip models following the M_w 6.4 foreshock and the mainshock are plotted as red dashed and solid blue curves, respectively.

mainshock occurred about 16 hours after the M_w 5.4 foreshock near its hypocenter (Fig. 6). It thus appears likely that the M_w 5.4 foreshock played a key role in triggering the mainshock. In this study, we assume that the M_w 5.4 event occurred on F1, though Shelly (2020) reported a northeastward lineation of aftershocks of the M_w 5.4 event and inferred the ruptured fault plane is the NE striking nodal plane orthogonal to F1. Dislocations on either nodal plane produce identical strain patterns, thus we cannot discriminate between these two possibilities from the strain observations. An alternative to the interpretation of Shelly (2020) is that the M_w 5.4 event ruptured on F1, yet triggered aftershocks on an orthogonal fault. Analysis related to the dynamic rupture directivity of the M_w 5.4 event may be important to determine its orientation. Jin and Fialko (2020) conducted a Coulomb stress calculation at 7 km depth and reported that the nucleation of the mainshock hypocenter may be discouraged by the M_w 5.4 event. Because the Coulomb stress varies significantly near the ruptured fault plane and the M_w 5.4 event is close to the mainshock hypocenter, the uncertainty related to its location, orientation, and dimension, as well as the uncertainty of mainshock hypocentral location need to be considered when evaluating the stress interactions between the M_w 5.4 event and the mainshock. Our analysis assumes that the M_w 5.4 event occurred on F1, but there is uncertainty in the mechanism and location of this event, which affects quantification of the triggering mechanism between the M_w 5.4 event and mainshock. Rupture during the M_w 6.4 event did not reach the northwest end of F1 and the seismic activity closest to the mainshock hypocenter was promoted by the M_w 5.4 event. The total moment release on F1 after the M_w 6.4 foreshock is dominated by the M_w 5.4 event, thus our interpretation is that it is likely that the M_w 5.4 event promoted the nucleation process of the mainshock due to its proximity and relative moment release.

The distinct slip behavior on F1 and F2 can be interpreted in the context of an “asperity model”. Asperities are portions of fault surfaces that are strongly locked during stress loading and rupture with large slip during earthquakes (e.g. Lay et al., 1982). Cascaded triggering can be produced by sequential rupturing of large asperities (Lay et al., 2012). The M_w 6.4 and 5.4 foreshocks ruptured different asperities on F1 (Fig. 6). Since the mainshock hypocenter is located close to the M_w 5.4 event and the slip on F1 is dominated by the seismic slip of the M_w 5.4 event, the sequen-

tial rupturing of asperities during the foreshocks appears to be the controlling mechanism of the foreshock to mainshock triggering on F1. The co-seismic slip distribution on F2 indicates that most asperities ruptured co-seismically, leaving the rest of the fault to displace in afterslip with a dominant component of aseismic slip. This phenomenon is further evident in the comparison of afterslip models following the M_w 6.4 foreshock and the mainshock.

3.3. Seismic vs. aseismic moment release of the orthogonal fault system

The FTI inversion results of the afterslip evolution are plotted in Fig. 7 in comparison with the co-seismic models. During the investigated period (July 5–Dec 31, 2019), considerable afterslip occurred with an equivalent slip moment of $M_w = 6.4$. On the main fault plane (M1), the afterslip forms a significant complementary pattern with the co-seismic slip. Most afterslip occurred near the two ends of M1 and is partially overlapped with aftershocks. The most significant afterslip occurred to the northwest of the co-seismic slip at ~ 20 km depth with a maximum slip of ~ 0.3 m. Shallow afterslip occurred above the major slip area of the mainshock, which is consistent with the shallow-slip deficit in the co-seismic model. Limited afterslip occurred beneath the co-seismic slip area. This pattern is validated with single fault plane inversion (only M1), single data type inversion, step displacement inversion, and inversions without viscous relaxation corrections, with the pattern holding up in all tests. Although stress changes are concentrated at the lateral ends and bottom edge of the co-seismic slip, lateral variation of rate-and-state dependent frictional properties may drive afterslip to be released faster on velocity strengthening patches. These patches commonly present “weak” frictional property and behave as barriers for dynamic ruptures. For example, the 2016 Kumamoto earthquake was stopped by the Aso volcano (Yue et al., 2017); meanwhile the volcano area presented significant afterslip and viscoelastic deformation (Moore et al., 2017). The 2019 Ridgecrest earthquake also stopped at the Coso geothermal area (Ross et al., 2019), where the most significant afterslip occurred. This observation resembles that of the 2016 Kumamoto earthquake and reflects the influence of a “barrier” introduced by velocity strengthening frictional properties.

The relative ratio of seismic versus aseismic slip is important for analyzing slip budget and future seismic hazard. We use the

earthquake catalog and slip models to represent the seismic versus total moment release on each fault plane. We assume events within 2 km from the fault plane occurred on the fault plane and share an identical focal mechanism, and the moment evolution is plotted in Fig. 7d. The afterslip models include all types of moment release on the fault plane, and we sum moments of all patches to calculate the total moment on each fault plane and scale the total moment by the source evolution function $S_0(t)$ to represent “total” release functions. Because the M_W 5.4 event was excluded from the strain time series when performing slip inversion for the period between the M_W 6.4 event and the mainshock, we assign the M_W 5.4 event slip model (Fig. S20) using a Heaviside (step) function and add that to the moment release function for F1. In Fig. 7d, the moment evolution in the first three days after the mainshock is plotted. The comparison of two moment evolution functions (from catalog and slip model) reveals distinct releasing patterns on parallel and orthogonal faults in both afterslip periods. For all the NW-trending faults (parallel faults including F1, M1, and M2), the seismic moment is comparable to the total moment in periods after the M_W 6.4 foreshock and the mainshock. Moments recovered by slip-models include both seismic and aseismic release, which is expected to be higher than pure seismic release. However, in the beginning epoch of the post-seismic period, the seismic moment increased faster than that of the slip model. This may be attributed to either off-fault aftershocks in the catalog being summed or the mechanism varies significantly in the catalog events, thus producing artificially high seismic moment summation. Although similar bias may hold for other fault planes, the seismic versus total moment history we observe on fault F2 (orthogonal faults) is distinct from that observed on NW-trending faults. The seismic moment accounted for is about 11% of the total moment from the slip models in afterslip following both the M_W 6.4 foreshock and the mainshock. This analysis clearly shows that dual slip modes are distinct on NW trending and SW trending faults. This phenomenon is also consistent with the cascade triggering mechanism of the fore-to-main-shock relationship. We also invert for the afterslip evolution using two processes. Though the “fast” and “slow” processes show clear spatial separation, it is not clear whether this effect is caused by uneven data coverage or by distinct physical processes. We include related discussion in the supplementary materials, yet cannot draw a definitive conclusion based on these analyses.

The seismic moment release didn't increase significantly after July 7th. Thus, it is anticipated that over a long-term (longer than about a week), the aseismic moment release would dominate on both fault systems. This phenomenon is consistent with the aseismic slip dominated post-seismic moment releases observed in many subduction zone earthquakes, e.g., the Maule earthquake (Lin et al., 2013), the Nias earthquake (Hsu et al., 2006), and the Tohoku earthquake (Diao et al., 2014). The exceptional observations of the Ridgecrest earthquake provide an opportunity to look into the very early post-seismic period, and we observe aseismic slip overtaking the seismic release several days after the mainshock. This indicates that the seismic response to the co-seismic shaking or stress changes associated with the cascade model may be a dominant factor in the early stage of post-seismic responses, while aseismic release account for a more important part over a longer time. The slow-slip driving model (Hsu et al., 2006; Perfettini et al., 2018) assumes afterslip drives aftershocks, which predicts that the cumulated number of aftershocks exhibit a similar evolution pattern as that of afterslip. In this study, we quantitatively compare the seismic versus total moment release in the post-seismic period, and the observed overtake pattern suggests that two competing mechanisms influence the aftershock sequence of the Ridgecrest earthquake; but in the early stage it is the earthquake rupture, not the slow-slip, that was the dominant driving mechanism.

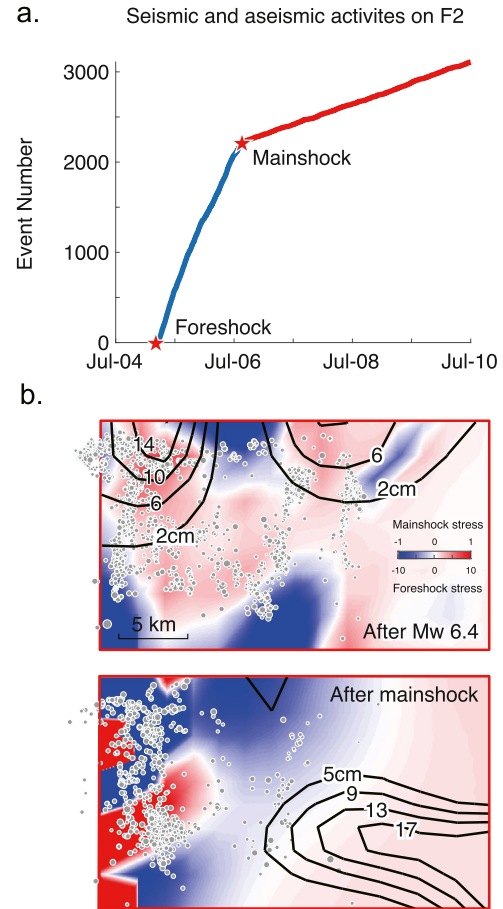


Fig. 8. Seismic and aseismic activities on F2 from the afterslip period following the M_W 6.4 foreshock and mainshock. **a.** The Cumulative number of foreshocks and aftershocks near fault F2 plotted as blue and red curves, respectively. **b.** Co-seismic Coulomb stress changes produced by the M_W 6.4 and mainshock are plotted in the top and bottom panels, respectively, using different color scales. Foreshocks and aftershocks on F2 are plotted as gray filled dots. Afterslip on F2 following the M_W 6.4 foreshock and the mainshock are plotted in the top and bottom panels, respectively.

3.4. Driving mechanism of afterslip following the M_W 6.4 foreshock and the mainshock

It has been noted that seismicity on F2 shows a significant decrease after the mainshock (<https://temblor.net/earthquake-insights/ridgecrest-earthquake-shut-down-cross-fault-aftershocks-9249/>), which drops from 1499 events per day during the period between the M_W 6.4 foreshock and the mainshock to 228 events per day within three days after the mainshock (Fig. 8). This sharp drop of seismicity appears to be counter-intuitive, because the mainshock is expected to cause a large stress change on F2. We calculated the Coulomb stress change produced by the M_W 6.4 foreshock and mainshock on F2, in which a frictional parameter of 0.4 was used to relate normal and shear stress changes. The Coulomb stress changes on F2 are calculated in reference to the M_W 6.4 foreshock slip direction, which is then compared with foreshock/aftershock activity and afterslip following the major events (Fig. 8). Foreshocks and aftershocks locate within the Coulomb stress increase areas produced by the M_W 6.4 foreshock and mainshock, respectively. These stress increase areas are also correlated with afterslip areas. The area at the center of F2 shows intensive foreshock activities, with both seismic and aseismic slip. This area is covered by a shadow of Coulomb stress decrease produced by the mainshock; thus, it seems the afterslip/aftershock activities are damped by mainshock stress changes. On the con-

trary, the Coulomb stress on the southwest end of F2 is elevated by both major events, thus is likely to increase afterslip. These comparisons indicate that co-seismic stress change may be an important factor controlling the slow-slip behaviors on F2. Thus the afterslip models can be used to investigate the frictional property of regional faults under some constitutive relationships relating to slow-slip velocity and stress changes. The rate-state friction laws may be a promising candidate to perform such an analysis.

Abundant aftershocks on orthogonal structures are reported for the Ridgecrest earthquake sequence, which draws attention to the aftershock hazard on such structures (e.g. Ross et al., 2019). In this study, we investigate moment release on these orthogonal structures and find that for the most significant SW-trending fault (F2), aseismic slip dominates the moment release in the period following the M_W 6.4 foreshock and the mainshock. Other SW-trending faults (A1 and A2) also present similar phenomena with significant afterslip ($M_W = 5.6$ for A1 and $M_W = 5.1$ for A2), although the seismic moments on these structures are difficult to quantify. Aseismic slip behavior may be a common feature for the SW-trending faults near the Ridgecrest earthquake.

The main fault (M1) shows limited co-seismic slip near the crossing point of these SW-trending faults. For example, the mainshock slip terminates at the junction between M1 and A1. Two voids of the mainshock slip are spatially correlated with cuts of off-fault structures (F2 and A3). For other strike-slip fault systems, the background seismicity on orthogonal or conjugate structures is also pervasive during the inter-seismic loading, such as the orthogonal faults near the San Jacinto fault, and the Xiaojiang Fault (Zhou et al., 2020). These observations indicate that stress is partially released on these perpendicular faults when the whole area is subject to shear loading in the inter-seismic period. The spatial and temporal clustering of these off-fault events indicates that they are likely to be driven by aseismic slip (Zhou et al., 2020). Thus these orthogonal structures regularly release stress loading and produce stress shadows on the main fault resulting in stress barriers (e.g., Yue et al., 2017). The relatively low rupture velocity of the Ridgecrest earthquake also indicates that the rupture encountered several barriers inhibiting continuous rupture. The feasibility of such fault interactive mechanisms requires validation by dynamic rupture modeling. The stress release behavior of these off-fault structures also requires creep-related dynamic fault modeling algorithms to validate.

The orthogonal fault system is the result of a unique tectonic environment in eastern California. The major slip on the NW trending fault produces plentiful small orthogonal faults in this broadened deformation zone, illuminated by the Ridgecrest earthquake sequence. Detailed afterslip data show quasi-regular spaced perpendicular strips along the M1 fault, implying the fault intercepting with multiple orthogonal weak fault segments. Wrench-style shear motions of the fault systems over geological time weakened the off-fault region and promoted secondary sub-parallel faults, producing a grid of faults/sub-faults as illuminated by the Ridgecrest earthquake sequence. This interpretation may also help our understanding of tectonic deformation in other parts of the world with orthogonal fault systems such as in SW China, where the Xiaojiang fault intercepts with the Red River fault, and produced the 1970 M_W 7.1 Tonghai earthquake.

4. Conclusions

We utilize the abundant seismic, geodetic, and strainmeter observations to construct a 3D fault model and co-seismic slip models and afterslip models following the M_W 6.4 foreshock and the mainshock to analyze the slip behavior and stress interactions of the Ridgecrest earthquake sequence. Our key findings include:

1. The M_W 6.4 foreshock ruptured an orthogonal fault system while the mainshock mainly ruptured a NW-trending fault. The foreshock, mainshock, and afterslip distributions have complementary slip distribution patterns on the fault planes.
2. The mainshock was likely triggered by the foreshock through a cascade of events on a short fault branch parallel to the main fault plane. The moment release on this fault is dominated by seismic slip. An M_W 5.4 event appears to be the key foreshock triggering the mainshock.
3. Overall slip on parallel and orthogonal faults involves different balances of seismic and aseismic slip. Seismic slip dominates the post-mainshock slip of the NW-trending faults, while aseismic slip dominates the post-foreshock slip on the SW-trending orthogonal fault. This is indicated by afterslip models following both the M_W 6.4 foreshock and the mainshock.
4. Abundant secondary orthogonal faults were activated during the Ridgecrest earthquake sequence. Their locations are correlated with gaps in the mainshock slip model. Seismic activities on the major north-east trending fault (F2) show significant change after two major events, which appear to be controlled by the stress change of two major events.

CRediT authorship contribution statement

The credit of authors is stated as follows:

Han Yue is in charge of Seismic data preparation, inversion, algorithm design and development, manuscript writing.
 Jianbao Sun is in charge of SAR data processing, inversion theory and scientific problem discussion.
 Min Wang is in charge of GPS data processing, inversion theory and scientific problem discussion.
 Zhengkang Shen is in charge of GPS data processing, inversion theory, tectonic and scientific problem discussion.
 Lian Xue is in charge of Strain data processing, inversion theory and scientific problem discussion.
 Weifan Lu and Yijian Zhou are in charge of seismicity detection.
 Chunmei Ren is in charge of regional velocity model extraction.
 Mingjia Li is in charge of post-seismic SAR time series processing.

Declaration of competing interest

The authors declare that they have no known competing financial interests or personal relationships that could have appeared to influence the work reported in this paper.

Data and materials availability

GPS data are recorded by plate boundary observatories (PBO) and made available by UNAVCO. The strong motion network is operated by Southern California Seismic Network (SCSN) (<https://authors.library.caltech.edu/34628/>) and made available by Southern California Earthquake Data Center at Caltech (SCEDC Caltech Dataset, <https://doi.org/10.7909/C3WD3xH1>). Strainmeters stations are operated by the GAGE facility and made available by UNAVCO. This work contains Copernicus data from the Sentinel-1 satellites provided by ESA, and ALOS-2 data from JAXA through ALOS-2 RA 6 project (PI No. 3381002).

Acknowledgements

We thank Prof. Shengji Wei for helping with the strong motion data processing, Lei Zhang from Hong Kong Polytechnic University and Jinghui Fan from China Geological Survey for helping on ALOS-2 data analysis. This work is supported by the National Key Research and Development Program of China (2018YFC1504203 H.Y.),

the National Natural Science Foundation of China (42021003 H.Y. & L.X., 41774043 J. S.), and the Dragon Project (32341 J.S.). Southern California Earthquake Center publication #XXXX. (Z.S.) and US National Science Foundation (EAR1802364 T. L.).

Appendix A. Supplementary material

Supplementary material related to this article can be found online at <https://doi.org/10.1016/j.epsl.2021.117066>.

References

- Bedford, J., Moreno, M., Baez, J.C., Lange, D., Tilmann, F., Rosenau, M., Heidbach, O., Oncken, O., Bartsch, M., Rietbrock, A., 2013. A high-resolution, time-variable afterslip model for the 2010 Maule $M_W = 8.8$, Chile megathrust earthquake. *Earth Planet. Sci. Lett.* 383, 26–36.
- Chen, K., Avouac, J.-P., Aati, S., Milliner, C., Zheng, F., Shi, C., 2020. Cascading and pulse-like ruptures during the 2019 Ridgecrest earthquakes in the Eastern California Shear Zone. *Nat. Commun.* 11, 1–8.
- Diao, F., Xiong, X., Wang, R., Zheng, Y., Walter, T.R., Weng, H., Li, J., 2014. Overlapping post-seismic deformation processes: afterslip and viscoelastic relaxation following the 2011 M_W 9.0 Tohoku (Japan) earthquake. *Geophys. J. Int.* 196, 218–229.
- Dieterich, J.H., 1979. Modeling of rock friction: 1. Experimental results and constitutive equations. *J. Geophys. Res., Solid Earth* 84 (B5), 2161–2168.
- Dokka, R.K., Travis, C.J., 1990. Role of the eastern California shear zone in accommodating Pacific-North American plate motion. *Geophys. Res. Lett.* 17, 1323–1326.
- DuRoss, C.B., Gold, R.D., Dawson, T.E., Scharer, K.M., Kendrick, K.J., Akciz, S.O., 2020 et al. Surface displacement distributions for the July 2019 Ridgecrest, California, earthquake ruptures. *Bull. Seismol. Soc. Am.* 110 (4), 1400–1418.
- Ellsworth, W.L., Bulut, F., 2018. Nucleation of the 1999 Izmit earthquake by a triggered cascade of foreshocks. *Nat. Geosci.* 11 (7), 531–535.
- Ende, M.P.A., Ampuero, J.-P., 2020. On the statistical significance of foreshock sequences in Southern California. *Geophys. Res. Lett.* 47, 3.
- Floyd, M., et al., 2020. Survey and Continuous GNSS in the vicinity of the July 2019 Ridgecrest earthquakes. *Seismol. Res. Lett.* 91, 2047–2054.
- Gan, W., Svarc, J.L., Savage, J., Prescott, W., 2000. Strain accumulation across the Eastern California Shear Zone at latitude 36° 30' N. *J. Geophys. Res., Solid Earth* 105, 16229–16236.
- Goldberg, D.E., Melgar, D., Sahakian, V.J., Thomas, A.M., Xu, X., Crowell, B.W., Geng, J., 2020. Complex rupture of an immature fault zone: a simultaneous kinematic model of the 2019 Ridgecrest, CA earthquakes. *Geophys. Res. Lett.* 47, e2019GL086382.
- Hartzell, S.H., Heaton, T.H., 1983. Inversion of strong ground motion and teleseismic waveform data for the fault rupture history of the 1979 Imperial Valley, California, earthquake. *Bull. Seismol. Soc. Am.* 73, 1553–1583.
- Hsu, Y.-J., Simons, M., Avouac, J.-P., Galetzka, J., Sieh, K., Chlieh, M., Natawidjaja, D., Prawirodirdjo, L., Bock, Y., 2006. Frictional afterslip following the 2005 Nias-Simeulue earthquake, Sumatra. *Science* 312, 1921–1926.
- Hough, S.E., Thompson, E., Parker, G.A., et al., 2020. Near-field ground motions from the July 2019 Ridgecrest, California, earthquake sequence. *Seismol. Res. Lett.* 91 (3), 1542–1555.
- Jin, Z., Fialko, Y., 2020. Finite slip models of the 2019 Ridgecrest earthquake sequence constrained by space geodetic data and aftershock locations. *Bull. Seismol. Soc. Am.* 110 (4), 1660–1679.
- Jones, L.M., Molnar, P., 1979. Some characteristics of foreshocks and their possible relationship to earthquake prediction and premonitory slip on faults. *J. Geophys. Res., Solid Earth* 84, 3596–3608.
- Kato, A., Obara, K., Igarashi, T., Tsuruoka, H., Nakagawa, S., Hirata, N., 2012. Propagation of slow slip leading up to the 2011 M_W 9.0 Tohoku-Oki earthquake. *Science* 335 (6069), 705–708.
- Kositsky, A., Avouac, J.P., 2010. Inverting geodetic time series with a principal component analysis-based inversion method. *J. Geophys. Res., Solid Earth* 115.
- Lay, T., Kanamori, H., Ammon, C.J., Koper, K.D., Hutko, A.R., Ye, L., Yue, H., Rushing, T.M., 2012. Depth-varying rupture properties of subduction zone megathrust faults. *J. Geophys. Res., Solid Earth* 117.
- Lay, T., Kanamori, H., Ruff, L., 1982. The asperity model and the nature of large subduction zone earthquakes. *EPR, Earthqu. Predict. Res.* 1, 3–71.
- Leprince, S., Barbot, S., Ayoub, F., Avouac, J.-P., 2007. Automatic and precise orthorectification, coregistration, and subpixel correlation of satellite images, application to ground deformation measurements. *IEEE Trans. Geosci. Remote Sens.* 45, 1529–1558.
- Lin, Y.-n.N., Sladen, A., Ortega-Culaciati, F., Simons, M., Avouac, J.-P., Fielding, E.J., Brooks, B.A., Bevis, M., Genrich, J., Rietbrock, A., Vigny, C., Smallley, R., Socquet, A., 2013. Co-seismic and post-seismic slip associated with the 2010 Maule Earthquake, Chile: characterizing the Arauco Peninsula barrier effect. *J. Geophys. Res., Solid Earth* 118, 3142–3159.
- Liu, X., Xu, W., 2019. Logarithmic model joint inversion method for co-seismic and post-seismic slip: application to the 2017 M_W 7.3 Sarpol Zahāb earthquake, Iran. *J. Geophys. Res., Solid Earth* 124 (11), 12034–12052.
- Liu, C., Lay, T., Brodsky, E.E., et al., 2019. Coseismic rupture process of the large 2019 Ridgecrest earthquakes from joint inversion of geodetic and seismological observations. *Geophys. Res. Lett.* 46 (21), 11820–11829. <https://doi.org/10.1029/2019GL084949>.
- Liu, S., Shen, Z., Bürgmann, R., Jónsson, S., 2020. A thin crème brûlée model for the Eastern California Shear Zone. *Geology*, in press.
- Magen, Y., Ziv, A., Inbal, A., Baer, G., Hollingsworth, J., 2020. Fault re-rupture during the July 2019 Ridgecrest earthquake pair from joint slip inversion of InSAR, optical imagery, and GPS. *Bull. Seismol. Soc. Am.* 110, 1627–1643.
- McClusky, S.C., Bjornstad, S., Hager, B.H., King, R., Meade, B.J., Miller, M., Monastero, F., Souter, B., 2001. Present day kinematics of the eastern California shear zone from a geodetically constrained block model. *Geophys. Res. Lett.* 28, 3369–3372.
- McLaskey, Gregory C., 2019. Earthquake initiation from laboratory observations and implications for foreshocks. *J. Geophys. Res., Solid Earth* 124 (12), 12882–12904.
- Miller, M.M., Johnson, D.J., Dixon, T.H., Dokka, R.K., 2001. Refined kinematics of the Eastern California shear zone from GPS observations, 1993–1998. *J. Geophys. Res., Solid Earth* 106, 2245–2263.
- Moreno, M., Rosenau, M., Oncken, O., 2010. 2010 Maule earthquake slip correlates with pre-seismic locking of Andean subduction zone. *Nature* 467, 198–202.
- Moore, J.D., Yu, H., Tang, C.-H., Wang, T., Barbot, S., Peng, D., Masuti, S., Dauwels, J., Hsu, Y.-J., Lambert, V., 2017. Imaging the distribution of transient viscosity after the 2016 M_W 7.1 Kumamoto earthquake. *Science* 356, 163–167.
- Perfettini, H., Frank, W.B., Marsan, D., Bouchon, M., 2018. A model of aftershock migration driven by afterslip. *Geophys. Res. Lett.* 45 (5), 2283–2293.
- Ross, Z.E., Idini, B., Jia, Z., Stephenson, O.L., Zhong, M., Wang, X., Zhan, Z., Simons, M., Fielding, E.J., Yun, S.-H., 2019. Hierarchical interlocked orthogonal faulting in the 2019 Ridgecrest earthquake sequence. *Science* 366, 346–351.
- Ruiz, S., Metois, M., Fuenzalida, A., Ruiz, J., Leyton, F., Grandin, R., Vigny, C., Madariaga, R., Campos, J., 2014. Intense foreshocks and a slow slip event preceded the 2014 Iquique M_W 8.1 earthquake. *Science* 345, 1165–1169.
- Savage, J., Lisowski, M., Prescott, W., 1990. An apparent shear zone trending north-northwest across the Mojave Desert into Owens Valley, eastern California. *Geophys. Res. Lett.* 17, 2113–2116.
- Schurr, B., Asch, G., Hainzl, S., Bedford, J., Hoechner, A., Palo, M., Wang, R., Moreno, M., Bartsch, M., Zhang, Y., 2014. Gradual unlocking of plate boundary controlled initiation of the 2014 Iquique earthquake. *Nature* 512, 299.
- Shelly, D., 2020. A high-resolution seismic catalog for the initial 2019 Ridgecrest earthquake sequence: foreshocks, aftershocks, and faulting complexity. *Seismol. Res. Lett.* 91 (4), 1971–1978.
- Shen, Z.K., Liu, Z., 2020. Integration of GPS and InSAR Data for Resolving 3-Dimensional Crustal Deformation. *Earth Space Sci.* 7, e2019EA001036.
- Shi, Q., Wei, S., Zeng, H., 2019. The 2019 Ridgecrest M_W 6.5 and M_W 7.0 double-let: shallow and slow rupture on non-planar strike-slip faults revealed by Multiple Point Source inversions using 3D Green's functions. In: AGU Fall Meeting.
- Strozzi, T., Kouraev, A., Wiesmann, A., Wegmüller, U., Sharov, A., Werner, C., 2008. Estimation of Arctic glacier motion with satellite L-band SAR data. *Remote Sens. Environ.* 112, 636–645.
- Trugman, D., Ross, Z.E., 2019. Pervasive foreshock activity across southern California. *EarthArXiv*. Jun 22.
- Unruh, J., Humphrey, J., Barron, A., 2003. Transtensional model for the Sierra Nevada frontal fault system, eastern California. *Geology* 31, 327–330.
- Wang, K., Dreger, D.S., Tinti, E., Bürgmann, R., Taira, T., 2020. Rupture process of the 2019 Ridgecrest, California M_W 6.4 foreshock and M_W 7.1 earthquake constrained by seismic and geodetic data. *Bull. Seismol. Soc. Am.* 110, 1603–1626.
- Wang, R., Lorenzo-Martín, F., Roth, F., 2006. PSGRN/PSCMP—a new code for calculating co- and post-seismic deformation, geoid and gravity changes based on the viscoelastic-gravitational dislocation theory. *Comput. Geosci.* 32, 527–541.
- Yoon, C.E., Yoshimitsu, N., Ellsworth, W.L., Beroza, G.C., 2019. Foreshocks and mainshock nucleation of the 1999 M_W 7.1 Hector Mine, California Earthquake. *J. Geophys. Res., Solid Earth* 124 (2), 1569–1582.
- Yue, H., Ross, Z.E., Liang, C., Michel, S., Fattahi, H., Fielding, E., Moore, A., Liu, Z., Jia, B., 2017. The 2016 Kumamoto $M_W = 7.0$ earthquake: a significant event in a fault–volcano system. *J. Geophys. Res., Solid Earth* 122, 9166–9183.
- Yue, H., Zhang, Y., Ge, Z., Wang, T., Zhao, L., 2020. Resolving rupture processes of great earthquakes: reviews and perspective from fast response to joint inversion. *Sci. China Earth Sci.* 63, 492–511.
- Zhou, Y., Yue, H., Zhou, S., Zhao, L., Yang, Z., Yao, Y., 2020. Weak off-fault structures revealed by micro-seismicity along Xiaojiang Fault Zone (China) and their implications for seismic hazard assessment. *J. Geophys. Res., Solid Earth*, submitted for publication.